ChemPubSoc Europe

DOI: 10.1002/cssc.201701565

CHEMSUSCHEM Full Papers

Cationic Vacancy Defects in Iron Phosphide: A Promising Route toward Efficient and Stable Hydrogen Evolution by Electrochemical Water Splitting

Wai Ling Kwong,*[a, b] Eduardo Gracia-Espino,[c] Cheng Choo Lee,[d] Robin Sandström,[c] Thomas Wågberg,[c] and Johannes Messinger*[a, b]

Engineering the electronic properties of transition metal phosphides has shown great effectiveness in improving their intrinsic catalytic activity for the hydrogen evolution reaction (HER) in water splitting applications. Herein, we report for the first time, the creation of Fe vacancies as an approach to modulate the electronic structure of iron phosphide (FeP). The Fe vacancies were produced by chemical leaching of Mg that was introduced into FeP as "sacrificial dopant". The obtained Fe-vacancy-rich FeP nanoparticulate films, which were deposited on Ti foil, show excellent HER activity compared to pristine FeP and Mg-doped FeP, achieving a current density of 10 mA cm^{-2} at overpotentials of 108 mV in 1 M KOH and 65 mV in 0.5 M H_2SO_4, with a near-100% Faradaic efficiency. Our theoretical and experimental analyses reveal that the improved HER activity originates from the presence of Fe vacancies, which lead to a synergistic modulation of the structural and electronic properties that result in a near-optimal hydrogen adsorption free energy and enhanced proton trapping. The success in catalytic improvement through the introduction of cationic vacancy defects has not only demonstrated the potential of Fe-vacancy-rich FeP as highly efficient, earth abundant HER catalyst, but also opens up an exciting pathway for activating other promising catalysts for electrochemical water splitting.

Introduction

A clean and renewable fuel based on molecular hydrogen (H_2) is regarded as a solution to multiple global challenges, including meeting the ever-increasing energy demand, the reduction of fossil fuel consumption and mitigating climate change. One appealing pathway to H_2 production is through water electrolysis driven by renewable energy sources such as solar and wind power. The implementation of this technology at a global scale is, however, hampered by the high cost and scarcity of noble metals such as Pt, Ir, and Ru, which presently are the best-known catalysts for efficiently and stably performing the two half-reactions of water splitting, that is, the hydrogen evolution reaction (HER) and the oxygen evolution reaction (OER). It is, therefore, imperative to develop earth-abundant catalysts that are catalytically as competent as noble-metal catalysts and that can be synthesized using scalable methods.

Recent intensive research has resulted in the development of promising alternatives to Pt as HER catalysts, including transition metal selenides,[1] sulfides,[2] carbides,[3] and phosphides.[4] Among these, the transition metal phosphides (TMPs) have emerged as one of the best candidates owing to their merits in catalytic activity and stability. On the basis of theoretical calculations, their efficiency in HER has been attributed to ensemble effects of phosphorus incorporation.[5] Phosphorus first dilutes the concentration of metal sites and thereby prevents catalytic deactivation caused by slow HER kinetics due to too strong binding of hydrogen to the metal sites, and second, it creates metal–phosphorus sites that bind hydrogen moderately and thus allow facile H_2 desorption. The H affinity to the catalytic surface and thus the resultant catalytic activity may be further tuned by engineering the material compositions of TMPs by doping, which further modulates the geometric and electronic structures of the material. Indeed, alloy catalysts pre-

[a] Dr. W. L. Kwong, Prof. J. Messinger
Department of Chemistry, Umeå University
Kemiskt Biologiskt Centrum (KBC)
90187 Umeå (Sweden)
E-mail: wailing.kwong@kemi.uu.se
johannes.messinger@umu.se

[b] Dr. W. L. Kwong, Prof. J. Messinger
Department of Chemistry-Ångström Laboratory
Molecular Biomimetics, Uppsala University
75120 Uppsala (Sweden)

[c] Dr. E. Gracia-Espino, R. Sandström, Prof. T. Wågberg
Department of Physics, Umeå University
90187 Umeå (Sweden)

[d] Dr. C. C. Lee
Umeå Core Facility for Electron Microscopy
Umeå University
90187 Umeå (Sweden)

Supporting Information and the ORCID identification number(s) for the author(s) of this article can be found under https://doi.org/10.1002/cssc.201701565.

This publication is part of a Special Issue on the topic of Artificial Photosynthesis for Sustainable Fuels. To view the complete issue, visit: http://dx.doi.org/10.1002/cssc.v10.22.

pared by cationic and/or anionic doping of TMPs often exhibit enhanced HER activity compared to their undoped counterparts.[4a–d, 6]

Another promising strategy for tailoring the catalyst composition toward improved catalytic properties is through the creation of vacancy defects. This strategy has shown promising results in both OER (Co_3O_4, $CoSe_2$, and Ir–Ni oxide)[7] and HER catalysts (MoS_2 and WSe_2),[1–2] in which the vacancies are found to catalytically activate neighboring atoms and/or improving the interfacial charge transfer. Nonetheless, the studies of vacancy defects for HER catalysts are scarce and are limited to anionic vacancies.[1–2]

Motivated by these studies, we investigate here the effect of cationic vacancy defects on the HER activity of FeP. Our theoretical calculations show that Mg doping and its subsequent removal for creating Fe vacancies indeed optimize the hydrogen adsorption free energy, suggesting that such materials will have higher catalytic activities. To demonstrate this experimentally, we developed a simple chemical treatment to create Fe vacancies in FeP. This method introduces Mg as sacrificial dopant, which is subsequently removed in a post-synthesis step by acid treatment. Electrochemical, structural, and mass spectrometric characterizations of these materials show that the Fe-vacancy-rich FeP exhibits a remarkable intrinsic catalytic activity and stability with high Faradaic efficiency for HER in both alkaline and acidic electrolytes.

Results and Discussion

To create Fe vacancies in the FeP catalyst, we selected Mg as sacrificial dopant owing to i) its earth abundance; ii) similarity (~9% difference) in ionic radius (0.086 nm) to that of Fe (0.0785 nm),[8] which would likely result in substitutional doping in FeP with minimal crystal distortion; and iii) ease of dissolution in acidic media (for the purpose of creating cationic vacancies). A low Mg content of 10 at.% (based on the total metal content, i.e., Mg/(Mg+Fe)) was chosen to minimize crystal distortion caused by its subsequent removal. The ab initio theoretical study on pristine FeP, Mg-doped FeP (Mg-FeP), and Fe-vacancy-rich FeP (Vc-FeP) systems is presented first to provide insights into the roles of Mg dopants and Fe vacancies on the HER activity, followed by the experimental results of the synthesized electrodes.

Theoretical results

The HER involves proton discharge leading to the adsorption of the hydrogen atom on the catalyst surface and its subsequent desorption through a chemical or electrochemical reaction to form H_2.[9] Here, the strength of the catalyst–hydrogen atom interaction dictates the limiting step and hence the catalytic activity. An ideal catalyst would interact with hydrogen atoms neither too weakly nor too strongly, so that the adsorption and desorption reactions have comparable energy barriers. In other words, an optimal HER kinetics is achieved at a thermoneutral Gibbs free energy, that is, $\Delta G_{H^*} = G_{H^*} - G_{1/2H_2} = 0$ eV, where G_{H^*} and $G_{1/2H_2}$ are the free energy of an H atom as adsorbed intermediate and desorbed in the gas phase, respectively.[1–2, 5–6, 10]

To calculate the H binding affinity of the surfaces of our three catalyst systems, we selected the (111) and (112) crystal plane as representative catalyst surfaces. As a similar trend is observed for these planes, only the (111) plane is described in detail whereas the results for the (112) surface are presented in the Supporting Information (Figure S3 and Table S2). Then, 10 at.% of Fe in FeP was replaced by Mg (i.e., Mg/(Mg+Fe) = 10 at.%) as a dopant to create Mg-FeP. Mg was subsequently removed from the structures to create the Fe vacancies in Vc-FeP. To account for inhomogeneity in doping and vacancy distribution, we prepared two Mg-FeP and two Vc-FeP systems for each crystalline surface, and three reaction sites per system were studied. The optimized configurations are depicted in Figure S1.

Despite the generally good catalytic activity of FeP reported in the literature,[11] we observe in our calculations for pristine FeP that its ΔG_{H^*} is well above 0, where the most active site has a $\Delta G_{H^*} = +0.16$ eV (see Table S1 and Figure 1a), indicating a weak surface interaction with H atoms and hence that the adsorption event might be the rate-limiting step for catalysis. Therefore, its catalytic activity can be improved by increasing the H affinity to the surface. Our calculations show that the addition of Mg decreases the ΔG_{H^*} 3-fold to +0.05 eV, suggesting a stronger hydrogen interaction. For Vc-FeP, the hydrogen in-

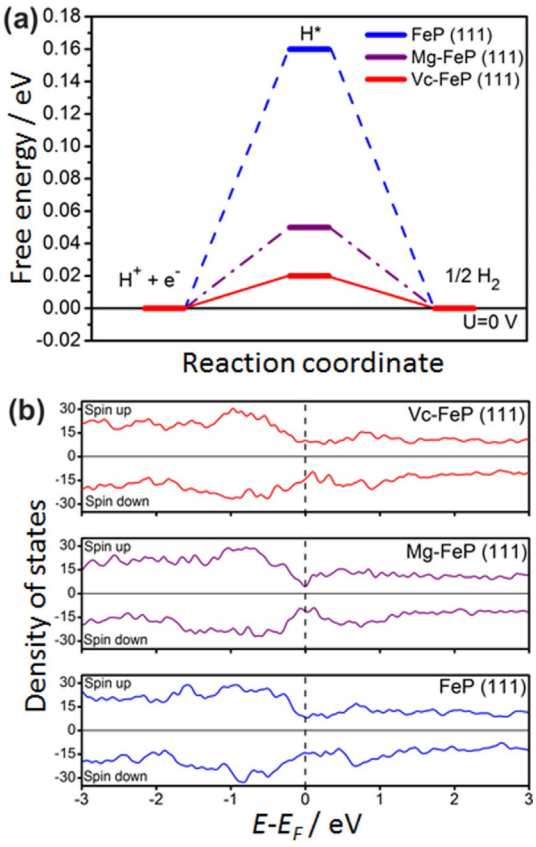

Figure 1. (a) Free energy diagram and (b) density of states of FeP, Mg-FeP and Vc-FeP (111) surfaces. Vertical dashed lines in (b) indicate the Fermi level.

teraction improves even further to $\Delta G_{H^*} = +0.02$ eV. Similar results are obtained also for the (112) surface (see Figure S2 and Table S1). Although $\Delta G_{H^*} > 0$ is normally associated with weak H–catalyst interactions, that is, the adsorption event being the limiting step, at such small values of ΔG_{H^*} for Mg-FeP and Vc-FeP, diverse factors (e.g., solvent effects) might easily reverse the sign of the calculated free energy. Therefore, the adsorption or desorption events could be the rate-limiting reaction. The near-zero ΔG_{H^*} for Vc-FeP suggests a low activation energy barrier for HER,[12] indicating that HER may occur on the catalyst surface at a low overpotential. Table S1, which lists also other sites with promising catalytic activity, shows clearly that Mg-FeP and Vc-FeP exhibit generally a stronger hydrogen interaction than pristine FeP. Because the difference in the spatial density of reaction sites also affects the HER activity, we estimated the reaction site density at a cutoff $\Delta G_{H^*} = \pm 0.2$ eV, and found that Vc-FeP has the highest number of 11 sites nm^{-2} compared to 8 sites nm^{-2} for Mg-FeP and 3 sites nm^{-2} for FeP. We are aware that these numbers strongly depend on the surface termination as well as dopant and defect distributions, however, they provide an insight into the activation of the catalyst surface.

The improvements on the ΔG_{H^*} show that both Mg dopants and Fe vacancies are expected to improve the catalytic activity of FeP. Their roles are illustrated further by examining the structural properties. The Fe–P bond length in Mg-FeP and Vc-FeP is slightly decreased from 2.34 Å in pristine FeP to 2.32 and 2.30 Å, respectively (see Table S1). This is expected to increase the Fe and P orbital overlap with that of the adsorbed hydrogen atom (H*), thereby stabilizing the hydrogen on their surfaces. Furthermore, the creation of Fe vacancies yields a relatively P-rich environment in Vc-FeP compared to pristine FeP and Mg-FeP, where the P, which is partially negatively charged,[4b] facilitates proton trapping and thus improves the HER kinetics. Nonetheless, both doping and vacancy defects also are associated with drawbacks, such as a reduction of the electrical conductivity. This is observed by examining their electronic properties (Figures 1b and S3). FeP exhibits metallic characteristics in agreement with previous studies,[13] in which the density of states (DOS) around the Fermi level ($E-E_F=0$) arise mostly from the d-bands of Fe and the p-states of P. Overall, the DOS around the Fermi level of Mg-FeP and Vc-FeP are only slightly lower than FeP, indicating lowering of the electrical conductivity. Nevertheless, the drop is slightly larger for Mg-FeP than for Vc-FeP.

Experimental results

Using our recently reported two-step synthesis method, that is, spray pyrolysis deposition of metal oxide film followed by a low-temperature phosphidation (see the Experimental Section),[4b] we prepared, in a scalable way, pristine FeP and Mg-FeP films on Ti foil substrates. Fe vacancies for Vc-FeP were created by simply soaking Mg-FeP in 0.5 M H_2SO_4 for 15 min to leach Mg from Mg-FeP. During this process, H_2 gas was produced as detected using membrane-inlet mass spectroscopy (MIMS) (Figure S4). This observation is similar to those previously observed during acid corrosion of Mg alloys.[14] Scanning electron microscopy (SEM; Figure 2a–c) reveals that all samples consist of nanoparticulate films with minimal morphological differences. Detailed inspection shows that Vc-FeP consists of slightly smaller particles (average size 11 ± 2 nm) than pristine FeP (17 ± 7 nm) and Mg-FeP (18 ± 6 nm). The mass loading was found to be similar among the samples (1.1 mg cm^{-2} for FeP; 1.4 mg cm^{-2} for Mg-FeP; 1.2 mg cm^{-2} for Vc-FeP), facilitating a direct comparison of their catalytic activities. Elemental analysis by energy dispersive X-ray spectroscopy (EDS, Figure S5) shows that the relative P content (P/(P + Mg + Fe)) of pristine FeP, Mg-FeP, and Vc-FeP are 51, 51, and 53 at.%, respectively. Furthermore, Mg constitutes approximately 10 at.% of the total metal content in Mg-FeP (Figure S5b) whereas no Mg is detected for Vc-FeP (Figure S5c). Further elemental examination of Vc-FeP by X-ray photoelectron spectroscopy (XPS) also shows no Mg signal (data not shown), indicating a complete removal of Mg (the detection limit for EDS and XPS is 0.1–1 at.%) by the acid treatment.

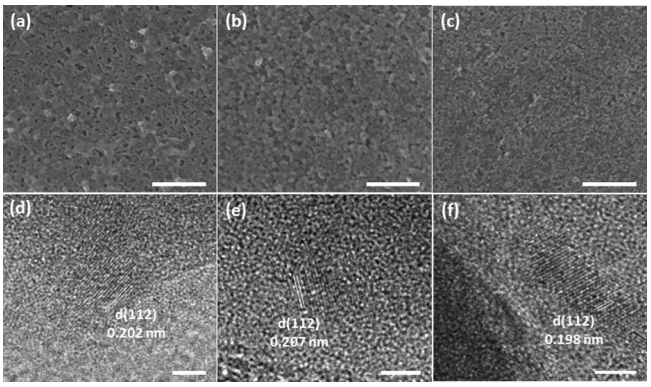

Figure 2. (a–c) Top-view SEM and (d–f) HRTEM images of (a, d) FeP, (b, e) Mg-FeP, and (c, f) Vc-FeP. Scale bar: (a–c) 200 nm, (d–f) 2.5 nm.

Figure S6 shows the X-ray diffraction (XRD) patterns of FeP, Mg-FeP, and Vc-FeP. All three samples exhibit broad diffraction peaks corresponding to the orthorhombic FeP phase.[15] The broad peaks indicate a low degree of crystallinity with small crystal grains. Additional peaks attributed to iron oxide are spotted in FeP. In our previous study,[4b] we demonstrated that the formation of iron oxide impurity can be suppressed by adding Ni dopant. This is also evidenced here, where the addition of Mg dopant inhibits the crystallization of iron oxide. Similar observations were reported in other systems including Zr-doped Ta_2O_5 and W-doped $Ge_2Sb_2Te_5$.[16] The absence of secondary XRD peaks owed to Mg in Mg-FeP suggests that the replacement of Fe by Mg occurs by substitutional doping. The broad diffraction peaks, however, render difficulty to precisely determine any peak shifts that may correspond to crystal distortions caused by the introduction or removal of Mg. Further analysis by high-resolution transmission electron microscopy (HRTEM) in Figure 2d–f show a lattice spacing of 0.202 nm in FeP, which is assigned to the (112) plane of orthorhombic FeP. A slight expansion in the lattice spacing to 0.207 nm is observed for Mg-FeP as a result of the larger ionic radius of Mg compared to Fe. When Mg is removed (Vc-FeP), the lattice

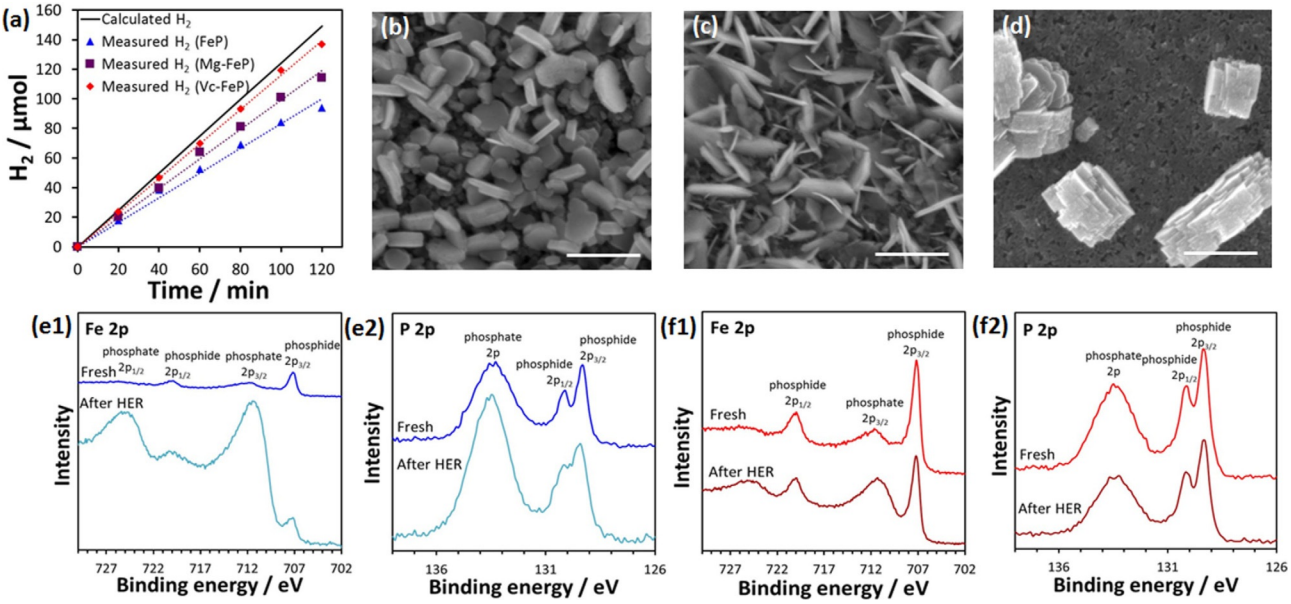

Figure 3. (a) Measurement of H_2 gas evolved in 1 M KOH. Top-view SEM images of (b) FeP, (c) Mg-FeP, and (d) Vc-FeP after the measurement. Scale bar in (b–d): 200 nm. Comparison of the XPS spectra for (e) FeP and (f) Vc-FeP before (fresh) and after the measurement. Assignment of peaks: (e1,f1) Fe $2p_{3/2}$ (707.2 eV) and Fe $2p_{1/2}$ (720.0 eV) of phosphide, Fe $2p_{3/2}$ (711.8 eV) and Fe $2p_{1/2}$ (725.3 eV) of phosphate;[11c,d,17] and (e2,f2) P $2p_{3/2}$ (129.5 eV) and P $2p_{1/2}$ (130.2 eV) of phosphide, P 2p of phosphate (133.5 eV).[11c,17a,18]

shrinks to 0.198 nm, indicating the formation of vacancy defects. The correlative analysis by EDS (Figure S7) shows a homogeneous elemental distribution in the samples.

We investigated the current-to-H_2 Faradaic efficiency of the samples in 1 M KOH by quantifying the gas evolved during 2 h of operation at a geometric current density (j_{geo}) of -10 mA cm^{-2}. As shown in Figure 3a, the average Faradaic efficiencies of FeP, Mg-FeP, and Vc-FeP are 70 ± 5%, 81 ± 3%, and 94 ± 2%, respectively. With a near-100% Faradaic efficiency, the charge passed in Vc-FeP is mostly consumed during HER. The comparatively low Faradaic efficiencies of FeP and Mg-FeP are owed to the formation of phosphate species on the surface. As observed in Figure 3b–d, the pristine nanoparticulate morphologies (Figure 2a–c) were transformed into sheet-like structures during the measurements. The amount of nanosheets on Vc-FeP is significantly lower than on FeP and Mg-FeP. These nanosheets were confirmed by XPS to be phosphate species, and the intensity of the peaks assigned to the phosphate phase for FeP (Figure 3e) and Mg-FeP (Figure S8) dramatically increased after the HER measurement. Such increment is considerably smaller for Vc-FeP (Figure 3f), suggesting that its high catalytic activity for HER outcompetes the rate of phosphate formation. According to a previous theoretical study,[13] the slightly higher P content of Vc-FeP, compared to FeP and Mg-FeP, may lead to an enhanced Fe–P covalent interaction, which further suppresses phosphate formation and provides catalytic stability. Although the mechanism of the phosphate formation under electroreductive conditions is unclear, it is possible that a portion of the charge passed was consumed by undesirable reduction of the dissolved O_2 in the electrolyte owing to the absence of an ion-conducting membrane between the anode and cathode compartments that would separate the gaseous products.[19] The reduction of O_2 could produce reactive oxygen species, which are the oxidizing agents possibly responsible for the formation of phosphate species.

The HER activities of FeP, Mg-FeP, and Vc-FeP were investigated further by measuring their polarization curves in 1 M KOH. Based on the results of the Faradaic efficiency measurement (Figure 3), some portion of the charge passed to the samples was consumed during phosphate formation. Therefore, to isolate the contribution of this unproductive side reaction from the measured current, we multiplied j_{geo} of the samples by their Faradaic efficiencies, viz., $j_{geo}\times$FE, (assuming that the measured Faradaic efficiencies are consistent up to $j_{geo}=-30$ mA cm^{-2} or within a potential window of 30 mV) and depicted the resulting polarization curves in Figure 4a. The bare Ti foil is catalytically inactive, producing negligible current in the investigated potential region. Among the samples, Vc-FeP exhibits the highest HER activity, and $j_{geo}\times\text{FE}=-10$ and -30 mA cm^{-2} are produced at overpotentials (η) as low as 108 and 139 mV, respectively. To achieve the same $j_{geo}\times$FE, Mg-FeP requires $\eta=149$ and 162 mV whereas FeP requires $\eta=192$ and 222 mV. The geometric HER activity of Vc-FeP is comparable to or even better than those recently reported nanostructured metal phosphide catalysts deposited on three-dimensional substrates (see Table S2), despite the advantage the latter have regarding having large real surface areas, which are expected to be associated with a high number of reaction sites per geometric area. Therefore, it is likely that the performance of Vc-FeP may be improved further by geometric area optimization. A comparison with Pt foil shows that Vc-FeP produces a higher $j_{geo}\times$FE at the high overpotential region ($\eta>135$ mV) (Figure 4a), implying its potential as a better catalyst at high current densities, which are often used in practical electrolyzer applications. The remarkable HER performance of Vc-FeP can be

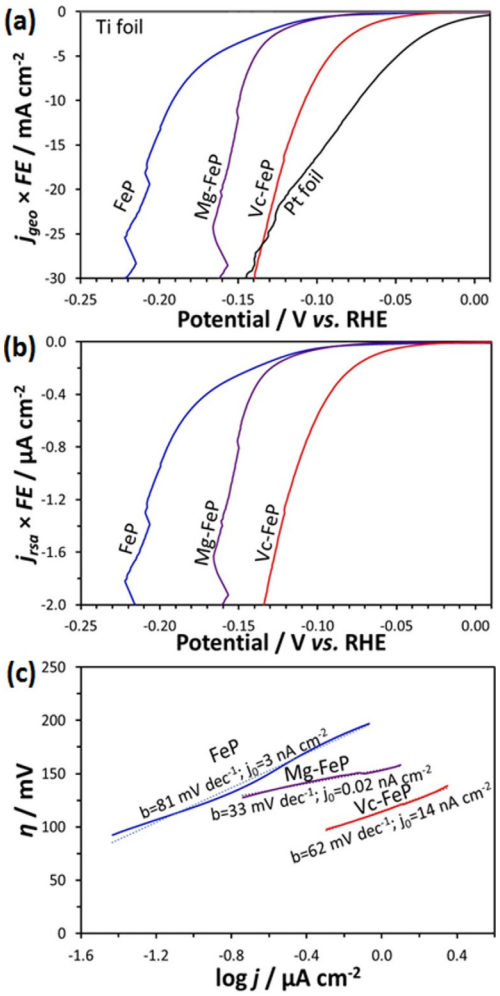

Figure 4. HER activity in 1 M KOH. Polarization curves, in which the current densities were multiplied by the Faradaic efficiency and normalized by (a) the electrode geometric area or by (b) the sample real surface area. (c) Tafel plots derived from (b). The curves in (a) and (b) appear jagged owing to interference of H_2 gas bubbles.

explained by detailed investigation of its intrinsic catalytic properties as presented below.

To obtain the intrinsic catalytic properties, the current measured in Figure 4a was normalized by the sample real surface area (rsa) to decouple the morphological effect (see the Experimental Section and Figure S13 for determination of rsa). The trend of the resultant current density (j_{rsa}×FE, Figure 4b) among the samples is the same as that of j_{geo}×FE, which indicates that the different overall HER activities of the samples in Figure 4a is mainly owed to their different intrinsic HER activities.

Tafel analyses were performed to obtain mechanistic insight into the effect of Mg dopants and Fe vacancies on the HER kinetics of FeP. As shown in Figure 4c, the extracted Tafel slope for FeP is 81 mV dec^{-1}, indicating that the rate of HER activity is limited by the electrochemical desorption of H_2.[9a] This is attributed to the low coverage by adsorbed hydrogen atoms on the FeP surface owing to the low H affinity as shown in our DFT results (Figure 1a). The comparatively higher H affinity on Mg-FeP and Vc-FeP surfaces increases the hydrogen atom coverage, which therefore is expected to increase the total amount of electrochemically desorbed H_2.and thus resulted in lower Tafel slopes of 33 and 62 mV dec^{-1}, respectively. The higher Tafel slope of Vc-FeP compared to that of Mg-FeP could be explained by its lower hydrogen coverage because the removal of Mg reduces the number of metal and/or metal–P binding sites.

The normalized exchange current density (j_0), obtained by extrapolating the Tafel plot in Figure 4c to the abscissa, follows the order of Vc-FeP (14 nA cm^{-2}) > FeP (3 nA cm^{-2}) > Mg-FeP (0.02 nA cm^{-2}). This order is consistent with the electrochemical impedance measured at $\eta = 0$ V (presented as Nyquist plots in Figure S9), in which interfacial charge-transfer resistance values of 0.3, 1.3, and 16.5 kΩ were obtained for Vc-FeP, FeP, and Mg-FeP, respectively. The lower j_0 of Mg-FeP compared to FeP could be owed to its lower electrical conductivity, as indicated by the lower DOS near the Fermi level (Figure 1b). This explains the need for activation by means of overpotential to drive the interfacial charge transfer for HER on the surface of Mg-FeP, despite of it having the lowest Tafel slope among the samples. Although the conductivity of Vc-FeP is slightly lower than that of FeP, its relatively P-rich environment (as determined by EDS in Figure S5) could enhance the proton trapping and thereby result in faster HER kinetics and hence higher j_0. That is, the optimized hydrogen-binding strength and the improved proton trapping are the likely reasons for the highest intrinsic HER activity of Vc-FeP among the samples.

In addition to catalytic activity, another essential quality of a HER catalyst is its stability in long-term operation to enable practical application in electrolyzers. We examined the operational stability of our best-performing sample, Vc-FeP in 1 M KOH through a continuous 1 day chronopotentiometic (CP) test at $j_{geo} = -10$ mA cm^{-2}. As shown in Figure 5a, η gradually increases and is stabilized at approximately 150 mV after 16 h of operation. The increase in η is owed to the surface formation of phosphate, as shown by the sheet-like morphology (Figure 5c) and the pronounced phosphate peak in the XPS spectra (Figure S10). Interestingly, the sample can be reactivated by electrochemical biasing ($j_{geo} = -10$ mA cm^{-2} for 30 min) in acid solution (0.5 M H_2SO_4), which results in the removal of phosphate species, as evidenced in the partial restoration of the catalyst surface to nanoparticulate morphology (Figure 5d) and in the increased phosphide peaks (Figure S10). The HER activity is then restored and further improved (Figure 5b). Although it has been reported that catalytic enhancement of an electrode after prolonged operation could be owed to Pt deposition on the electrode surface caused by the elution of Pt counter electrode,[20] we found no Pt impurity in the XPS spectrum (Figure S11) of Vc-FeP after the reactivation process. The improved HER activity is likely due to surface roughening after the removal of phosphate species, which exposes more active sites to the electrolyte. This reactivation cycle enables the reusability of the catalyst, thus significantly reducing the operational costs.

We further examined the HER activity of Vc-FeP in 0.5 M H_2SO_4, a highly acidic condition that is required for proton-exchange-membrane electrolyzers.[21] As shown in Figure 6a, Vc-FeP catalyzes the HER much more efficiently in acidic electrolyte, exhibiting a Tafel slope of 49 mV dec^{-1}, and $\eta = 65$ and

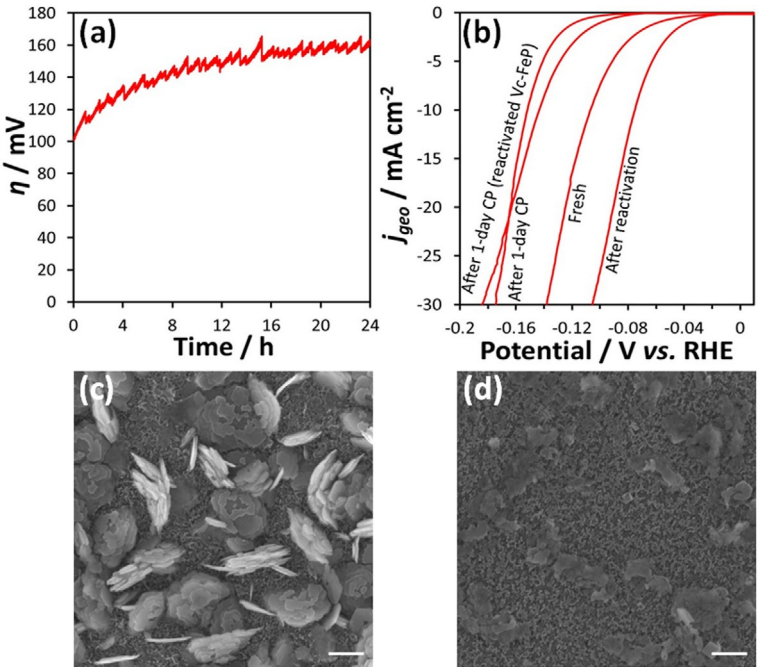

Figure 5. Stability test on Vc-FeP performed in 1 M KOH. (a) 1 day CP test at $j_{geo} = -10$ mA cm^{-2}. (b) Comparison of the polarization curves recorded before (fresh) and after the 1 day CP test, followed by the reactivation and another 1 day CP test. Top-view SEM images (c) after the 1 day CP test and (d) after the reactivation. Scale bar in (c–d) 200 nm. The curve in (a) appears jagged owing to interference of H_2 gas bubbles.

92 mV at $j_{geo} = -10$ and -30 mA cm^{-2}, respectively. This excellent HER performance is on par with or even surpasses many state-of-the-art nanostructured metal phosphide catalysts (Table S3). A Faradaic efficiency of 101 ± 6% (Figure 6b) shows that no side reactions are occurring and that all charges are consumed exclusively during HER. During a continuous 7 day CP test at $j_{geo} = -10$ mA cm^{-2} (Figure 6c), Vc-FeP demonstrates a remarkable catalytic stability with a slight deterioration, where the η required to generate $j_{geo} = -10$ mA cm^{-2} increases by only 18%. The catalyst surface morphology (Figure S12a) and crystal phase (Figure S12b) show negligible changes after the 7 days of operation.

Conclusions

We prepared a highly active hydrogen evolution reaction (HER) catalyst of Fe-vacancy-rich FeP nanoparticulate film using a facile and scalable sacrificial doping method. Fe vacancies were created in FeP by chemical leaching of Mg dopant from Mg-doped FeP. From theoretical predictions, the Fe-vacancy-rich FeP exhibited an optimal hydrogen adsorption free energy, which was attributed to the stronger hydrogen interaction and proton trapping compared to pristine and Mg-doped FeP. This was experimentally proven by its excellent HER activity in both alkaline and acidic electrolytes, achieving a current density of -10 mA cm^{-2} at low overpotentials of 108 and 65 mV, respectively. It also delivered a near-100% Faradaic efficiency and a good operational stability (at least 1 day in 1 M KOH and 7 days in 0.5 M H_2SO_4). The versatile approach of combining cationic doping and post-synthesis chemical treatment could be an effective strategy for creating cationic vacancies as active sites in a broad range of catalysts for HER and other electrocatalytic applications.

Experimental Section

Chemicals

All chemicals purchased were used without further purification: $FeCl_3 \cdot 6H_2O$ (≥99%; Sigma–Aldrich), $MgCl_2 \cdot 6H_2O$ (≥99%; Scharlau), $NaH_2PO_2 \cdot H_2O$ (≥99%; Sigma–Aldrich), Ti foil (99%; 0.127 mm thick; Alfa Aesar), H_2SO_4 (95–97%; Merck), and KOH (85.6%; VWR BDH Prolabo).

Synthesis of iron-based phosphides

Iron-based oxide films were prepared by spray pyrolysis deposition on Ti foils (substrate; heated on a hotplate to 350 °C) from metal chloride spray solutions with 0.05 M metal concentration. For Mg doping, the spray solutions contained 0.04 M Fe and 0.01 M Mg. The spray nozzle was tilted 45° and placed at 45 cm from the Ti foil. Compressed air (0.5 bar) was used to carry the aerosol at a flow rate of 11.5 mL min^{-1}. The deposition was completed after 4 cycles of 4 min spray with 1 min break taken between cycles to allow the restoration of the hotplate temperature to 350 °C. Subsequently, the film (geometric area = 1 × 2 cm^2) was heated using an isomantle at 450 °C for 30 min, in a sealed flask that contained $NaH_2PO_2 \cdot H_2O$ (0.027 g) and under a static Ar atmosphere [Caution: heating $NaH_2PO_2 \cdot H_2O$ releases toxic PH_3 gas that self-ignites in air; this reaction should be performed under air-free conditions]. After cooling naturally to room temperature, the samples were collected, rinsed with distilled water, and dried in air. To prepare Mg-leached film, the Mg-doped film was soaked in 0.5 M H_2SO_4 for 15 min and subsequently rinsed with distilled water and dried in air.

Characterizations

Field-emission SEM (FESEM; view at 5 kV operating voltage) and EDS were performed using Carl Zeiss Merlin equipped with X-Max 80 mm^2 Oxford Instruments. XRD was done using Bruker D8 Ad-

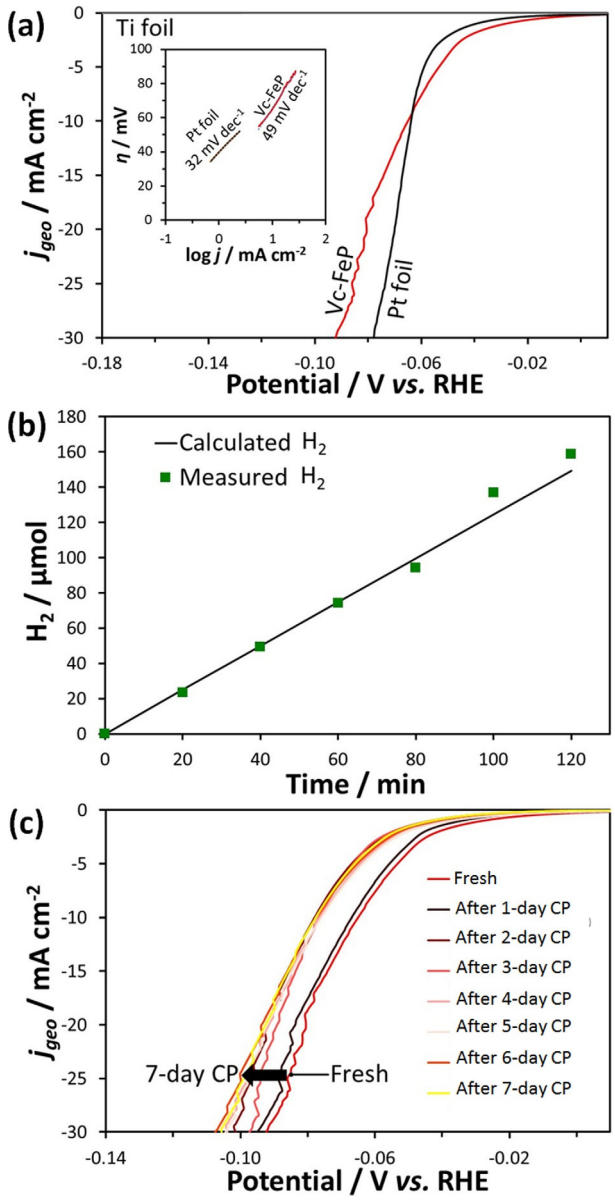

Figure 6. HER activity of Vc-FeP in 0.5 M H_2SO_4. (a) Polarization curves and corresponding Tafel plots (inset). (b) H_2 gas measurement. (c) Comparison of the polarization curves taken after cumulative 1 day CP tests ($j_{geo} = -10$ mA cm^{-2}), which sums up to 7 days. The curves in (a) and (c) appear jagged owing to interference of H_2 gas bubbles.

vance (CuK$_\alpha$ radiation at 40 kV and 40 mA). High-resolution XPS were collected using a Kratos Axis Ultra DLD spectrometer with a monochromatic AlK$_\alpha$ source. HRTEM was done using a Schottky field-emission electron microscope (JOEL JEM-2100F) operated at 200 kV equipped with a Gatan Ultrascan 1000 CCD camera and a postcolumn imaging filter. The samples for HRTEM were prepared by dispersing the film in distilled water for 24 h using an ultrasonicator and subsequently drop-casting the dispersion onto a TEM Cu grid with carbon supporting film and drying in air.

Electrochemical measurements for HER

A typical three-electrode electrochemical cell was used, where the sample, a Pt coil, and a Ag/AgCl/1 M KCl constituted the working, counter, and reference electrodes, respectively. All three electrodes were immersed in a Teflon cell, which contained 1 M KOH (pH 14) or 0.5 M H_2SO_4 (pH 0.3) as the electrolyte. The geometric area of the sample that was exposed to the electrolyte was defined by the diameter of an O-ring, which was approximately 0.2 cm^2. Linear sweep voltammetries (LSV) were collected at a scan rate of 2 mV s^{-1} in the cathodic direction and subsequently subtracted from the capacitive baseline to decouple the background capacitive current. Cyclic voltammetries (CV) were recorded at 10–50 mV s^{-1}, starting in the cathodic direction, in a 0.1 V window centered at the open-circuit potential. All potentials (E) reported herein were referenced to the reversible hydrogen electrode (RHE) by U(vs. RHE) = U(vs. Ag/AgCl)+0.222 V+(0.059×pH) and were corrected for uncompensated cell resistance, which was determined by electrochemical impedance spectroscopy. The real surface areas of the samples were estimated by measuring the double-layer capacitance using CV (Figure S13). The slope of the plot of $\Delta j/2$ (Δj is the difference between the anodic and the cathodic current densities at open-circuit potential) as a function of potential scan rate yielded the value for the double-layer capacitance, which was compared to the capacitance of a flat surface (0.04 mF cm^{-2}).[9a, 22]

For quantification of the H_2 gas evolved, a gas-tight, two-compartment electrochemical cell was used to house the three electrodes, where the working and reference electrodes were kept in the main compartment that was separated from the counter electrode by a glass frit. Prior to the measurements, the electrolyte and the headspace in the cell were purged with N_2 gas and examined for gas-tightness for 1 h. Aliquots of the gas in the headspace of the main compartment were extracted at 20 min intervals during a 2 h CP (fixed current density of −10 mA cm^{-2}) for analysis using MIMS (ThermoFinnigan Delta plus XP). Known amounts of 0.5% H_2/Ar gas mixture (±2% relative uncertainty; AGA AB) were used to calibrate the sensitivity of MIMS toward H_2. The amount of H_2 evolved was the sum of the gas in the headspace and the gas dissolved in the electrolyte, which was calculated using the Henry constant (7.8 µmol m^{-3} Pa^{-1} for H_2).[23]

Computational details

Spin-polarized calculations were performed using DFT within the generalized gradient approximation. The exchange-correlation potential was determined using the revised Perdew–Burke–Ernzerhof (RPBE)[24] model as implemented in the SIESTA code.[25] Wave functions for the valence electrons are represented by a linear combination of pseudo-atomic numerical orbitals using double-ζ plus one polarized orbital basis. The FeP with the space group *Pbnm* was used as starting configuration, for which the bulk lattice parameters obtained from our DFT calculations are a = 5.822 Å, b = 5.267 Å, and c = 3.133 Å, which are in good agreement with the experimental values (a = 5.793 Å, b = 5.187 Å, c = 3.093 Å).[26] Subsequently, (111) and (112) FeP surfaces were created by constructing FeP slabs with thickness of ~12 Å. For each crystalline surface, three different systems were built: Pristine FeP (FeP), Mg-doped FeP (Mg-FeP), and Fe-vacancy-rich FeP (Vc-FeP). For the Mg-FeP and Vc-FeP systems, two replicas with different atomic configurations were also studied, resulting in a total of 10 systems. A variable cell optimization without any constrains was performed before any adsorption event. The real-space grid used for charge and potential integration is equivalent to a plane wave cutoff energy of 300 Ry. The sampling of the Brillouin zone was performed with 3×3×1 Monkhorst–Pack grid and the force tolerance was set to 0.04 eV Å^{-1}. A k grid of 16×16×1 was used for the density of states.

The HER was studied with DFT using the computational hydrogen electrode (CHE) model as proposed by Nørskov et al.[27] The total HER can be written as $H^+ + e^- \rightarrow 1/2\,H_2$, and by specifying standard conditions (pH 0 in the electrolyte and 1 bar of H_2 in the gas phase at 298.15 K) the chemical potential of a proton–electron pair ($H^+ + e^-$) in solution is equal to half of the chemical potential of a gas-phase H_2 molecule. In this way, we avoid to treat explicitly solvated protons, and instead only the gaseous hydrogen molecule is required and easily computable using DFT. Additionally, at the equilibrium potential ($U = 0$ V), the free energy of the initial and final state are the same. The Gibbs free energy of the adsorbed state is then defined as $\Delta G_{H^*} = G_{H^*} - G_{1/2H_2}$, where it can be expressed also as $\Delta G_{H^*} = \Delta E_H + \Delta E_{ZPE} - T\Delta S_H$, where ΔE_H is determined as the energy difference between the adsorbed H atom and the gas phase H_2 molecule ($\Delta E_H = E_{surf+H} - E_{surf} - {}^1/_2\,E_{H_2}$), ΔE_{ZPE}, and $T\Delta S_H$ are the differences in zero-point energy and entropy between the adsorbed and the gas phase, estimated to be 0.14 eV for HER.[28] Therefore, an endergonic process ($\Delta G_{H^*} > 0$) indicates that the adsorption process is the limiting step, whereas an exergonic process ($\Delta G_{H^*} < 0$) suggests that the hydrogen desorption is the bottleneck. Thus, ΔG_{H^*} is a measurement of the reaction feasibility where a thermoneutral process ($\Delta G_{H^*} = 0$) is the most beneficial case. Note that this approach does not consider the energy barriers between intermediates from solvent reconstruction; as a result, the change in free energy only indicates if a reaction is thermodynamically allowed. The HER was studied on 3 different active sites per surface.

Acknowledgements

This work was supported by the Strong Research Environment Solar Fuels (Umeå University), the Artificial Leaf Project Umeå (Knut & Alice Wallenberg foundation; KAW 2011.0055), and Energimyndigheten (36648-1). We are thankful for the support from the Umeå Core Facility for Electron Microscopy (UCEM), the X-ray Photoelectron Spectroscopy laboratory at the Chemical Biological Centre (KBC), and the X-ray laboratory at the Department of Applied Physics and Electronics at Umeå University. We also thank Andrey Shchukarev for the XPS measurements. E.G.E. acknowledges support from the Carl Tryggers Foundation (CTS-16–161). The theoretical simulations were performed on resources provided by the Swedish National Infrastructure for Computing (SNIC) at the High Performance Computing Center North (HPC2N).

Conflict of interest

The authors declare no conflict of interest.

Keywords: artificial photosynthesis · cation vacancy · iron phosphide · sacrificial dopant · solar fuels

[1] Y. Sun, X. Zhang, B. Mao, M. Cao, *Chem. Commun.* **2016**, *52*, 14266 – 14269.
[2] a) H. Li, C. Tsai, A. L. Koh, L. Cai, A. W. Contryman, A. H. Fragapane, J. Zhao, H. S. Han, H. C. Manoharan, F. Abild-Pedersen, J. K. Nørskov, X. Zheng, *Nat. Mater.* **2016**, *15*, 48 – 53; b) A.-Y. Lu, X. Yang, C.-C. Tseng, S. Min, S.-H. Lin, C.-L. Hsu, H. Li, H. Idriss, J.-L. Kuo, K.-W. Huang, L.-J. Li, *Small* **2016**, *12*, 5530 – 5537.
[3] F. Harnisch, G. Sievers, U. Schröder, *Appl. Catal. B* **2009**, *89*, 455 – 458.
[4] a) G. Zhang, G. Wang, Y. Liu, H. Liu, J. Qu, J. Li, *J. Am. Chem. Soc.* **2016**, *138*, 14686 – 14693; b) W. L. Kwong, C. C. Lee, J. Messinger, *J. Phys. Chem. C* **2017**, *121*, 284 – 292; c) A. Mendoza-Garcia, D. Su, S. Sun, *Nanoscale* **2016**, *8*, 3244 – 3247; d) J. Hao, W. Yang, Z. Zhang, J. Tang, *Nanoscale* **2015**, *7*, 11055 – 11062; e) H. Huang, C. Yu, J. Yang, X. Han, C. Zhao, S. Li, Z. Liu, J. Qiu, *J. Mater. Chem. A* **2016**, *4*, 16028 – 16035.
[5] P. Liu, J. A. Rodriguez, *J. Am. Chem. Soc.* **2005**, *127*, 14871 – 14878.
[6] a) T. Liu, X. Ma, D. Liu, S. Hao, G. Du, Y. Ma, A. M. Asiri, X. Sun, L. Chen, *ACS Catal.* **2017**, *7*, 98 – 102; b) H. Huang, C. Yu, C. Zhao, X. Han, J. Yang, Z. Liu, S. Li, M. Zhang, J. Qiu, *Nano Energy* **2017**, *34*, 472 – 480.
[7] a) Y. Wang, T. Zhou, K. Jiang, P. Da, Z. Peng, J. Tang, B. Kong, W.-B. Cai, Z. Yang, G. Zheng, *Adv. Energy Mater.* **2014**, *4*, 1400696; b) Y. Liu, H. Cheng, M. Lyu, S. Fan, Q. Liu, W. Zhang, Y. Zhi, C. Wang, C. Xiao, S. Wei, B. Ye, Y. Xie, *J. Am. Chem. Soc.* **2014**, *136*, 15670 – 15675; c) T. Reier, Z. Pawolek, S. Cherevko, M. Bruns, T. Jones, D. Teschner, S. Selve, A. Bergmann, H. N. Nong, R. Schlögl, K. J. J. Mayrhofer, P. Strasser, *J. Am. Chem. Soc.* **2015**, *137*, 13031 – 13040.
[8] R. D. Shannon, *Acta Crystallogr. Sect. A* **1976**, *32*, 751 – 767.
[9] a) B. E. Conway, B. V. Tilak, *Electrochim. Acta* **2002**, *47*, 3571 – 3594; b) C. G. Morales-Guio, L.-A. Stern, X. Hu, *Chem. Soc. Rev.* **2014**, *43*, 6555 – 6569; c) P. Xiao, W. Chen, X. Wang, *Adv. Energy Mater.* **2015**, *5*, 1500985.
[10] M. G. Walter, E. L. Warren, J. R. McKone, S. W. Boettcher, Q. Mi, E. A. Santori, N. S. Lewis, *Chem. Rev.* **2010**, *110*, 6446 – 6473.
[11] a) C. Y. Son, I. H. Kwak, Y. R. Lim, J. Park, *Chem. Commun.* **2016**, *52*, 2819 – 2822; b) C. C. Lv, Z. Peng, Y. X. Zhao, Z. P. Huang, C. Zhang, *J. Mater. Chem. A* **2016**, *4*, 1454 – 1460; c) Y. Yan, B. Y. Xia, X. M. Ge, Z. L. Liu, A. Fisher, X. Wang, *Chem. Eur. J.* **2015**, *21*, 18062 – 18067; d) R. Liu, S. Gu, H. Du, C. M. Li, *J. Mater. Chem. A* **2014**, *2*, 17263 – 17267.
[12] J. K. Nørskov, T. Bligaard, A. Logadottir, S. Bahn, L. B. Hansen, M. Bollinger, H. Bengaard, B. Hammer, Z. Sljivancanin, M. Mavrikakis, Y. Xu, S. Dahl, C. J. H. Jacobsen, *J. Catal.* **2002**, *209*, 275 – 278.
[13] J. Wu, X. Y. Chong, R. Zhou, Y. H. Jiang, J. Feng, *RSC Adv.* **2015**, *5*, 81943 – 81956.
[14] a) C. Gu, J. Lian, J. He, Z. Jiang, Q. Jiang, *Surf. Coat. Technol.* **2006**, *200*, 5413 – 5418; b) J.-Y. Uan, S.-H. Yu, M.-C. Lin, L.-F. Chen, H.-I. Lin, *Int. J. Hydrogen Energy* **2009**, *34*, 6137 – 6142.
[15] K. E. Fylking, *Ark. Kemi. Mineral. Geo.* **1934**, *11B*, 48.
[16] a) S. Guo, Z. Hu, X. Ji, T. Huang, X. Zhang, L. Wu, Z. Song, J. Chu, *RSC Adv.* **2014**, *4*, 57218 – 57222; b) J.-Y. Tewg, Y. Kuo, J. Lu, *Electrochem. Solid-State Lett.* **2005**, *8*, G27 – G29.
[17] a) V. V. Nemoshkalenko, V. V. Didyk, V. P. Krivitskii, A. I. Senkevich, *Zh. Neorg. Khim.* **1983**, *28*, 2182 – 2186; b) C. E. Myers, H. F. Franzen, J. W. Anderegg, *Inorg. Chem.* **1985**, *24*, 1822 – 1824.
[18] a) R. Franke, T. Chasse, P. Streubel, A. Meisel, *J. Electron Spectrosc. Relat. Phenom.* **1991**, *56*, 381 – 388; b) Y. Barbaux, M. Dekiouk, D. Lemaguer, L. Gengembre, D. Huchette, J. Grimblot, *Appl. Catal. A* **1992**, *90*, 51 – 60; c) M. Ledendecker, S. K. Calderon, C. Papp, H. P. Steinruck, M. Antonietti, M. Shalom, *Angew. Chem. Int. Ed.* **2015**, *54*, 12361 – 12365; *Angew. Chem.* **2015**, *127*, 12538 – 12542.
[19] a) X. Xu, C. Shi, R. Chen, T. Chen, *RSC Adv.* **2017**, *7*, 22263 – 22269; b) Y. Mu, Z. Ai, L. Zhang, *Environ. Sci. Technol.* **2017**, *51*, 8101 – 8109.
[20] a) G. Dong, M. Fang, H. Wang, S. Yip, H.-Y. Cheung, F. Wang, C.-Y. Wong, S. T. Chu, J. C. Ho, *J. Mater. Chem. A* **2015**, *3*, 13080 – 13086; b) R. Chen, C. Yang, W. Cai, H.-Y. Wang, J. Miao, L. Zhang, S. Chen, B. Liu, *ACS Energy Lett.* **2017**, *2*, 1070 – 1075.
[21] D. Bessarabov, H. Wang, H. Li, N. Zhao, *PEM Electrolysis for Hydrogen Production: Principles and Applications*, CRC, Boca Raton, FL, **2016**.
[22] a) D. C. Grahame, *Chem. Rev.* **1947**, *41*, 441 – 501; b) R. Kötz, M. Carlen, *Electrochim. Acta* **2000**, *45*, 2483 – 2498.
[23] R. Sander, *Atmos. Chem. Phys.* **2015**, *15*, 4399 – 4981.
[24] B. Hammer, L. B. Hansen, J. K. Nørskov, *Phys. Rev. B* **1999**, *59*, 7413 – 7421.
[25] J. M. Soler, E. Artacho, J. D. Gale, A. García, J. Junquera, P. Ordejón, D. Sánchez-Portal, *J. Phys. Condens. Matter* **2002**, *14*, 2745 – 2779.
[26] R. W. G. Wyckoff, *Crystal Structures*, Interscience Publishers, New York, **1963**.
[27] J. K. Nørskov, T. Bligaard, A. Logadottir, J. R. Kitchin, J. G. Chen, S. Pandelov, U. Stimming, *J. Electrochem. Soc.* **2005**, *152*, J23 – J26.
[28] R. Michalsky, Y.-J. Zhang, A. A. Peterson, *ACS Catal.* **2014**, *4*, 1274 – 1278.

Manuscript received: August 18, 2017
Revised manuscript received: September 25, 2017
Accepted manuscript online: October 5, 2017
Version of record online: October 27, 2017

